REGULARIZATION OF AN INVERSE PROBLEM IN REMOTE SENSING IMAGING BY APERTURE SYNTHESIS

Eric ANTERRIEU

Laboratoire d'Astrophysique de l'Observatoire Midi-Pyrénées
Université Paul Sabatier & CNRS - UMR5572
14, avenue Edouard Belin
31400 Toulouse - France

ABSTRACT

It is now well established that synthetic aperture imaging radiometers are powerful sensors for high-resolution observations of the Earth at low microwave frequencies. This article deals with the reconstruction of radiometric brightness temperature maps from interferometric measurements. The corresponding inverse problem is often ill-posed unless a regularizing constraint is introduced in order to provide a unique and stable solution. Standard regularizing approaches are presented, the corresponding solutions are analyzed and the links between their physical and mathematical meanings are established. To support the theory, numerical simulations are presented and analyzed with emphasis on stability and error analysis.

1. INTRODUCTION

Synthetic Aperture Imaging Radiometers (SAIR) are powerful instruments for high-resolution observation of planetary surfaces at low microwave frequencies. This article is devoted to the reconstruction of radiometric brightness temperature maps from SAIR interferometric measurements. It has been demonstrated that the corresponding inverse problem is not well-posed, unless a regularizing constraint is introduced in order to provide a unique and stable solution. Since SAIR belong to the family of band-limited imaging devices, such a physical property should certainly be taken into account in the regularization of the imaging problem. However, other regularizing methods could achieve the same results, even if their physical meaning is somewhere hidden by the mathematical foundations. This contribution makes a review of standard methods for the regularization of inverse problems in imaging radiometry by aperture synthesis: the regularized solutions in the sense of Tikhonov, the solutions with minimal energy and those with band-limited properties are analyzed and the links between their physical and mathematical meanings are established. To support the theory, numerical simulations are presented within the frame of the SMOS space mission, a project led by the European Space Agency and devoted to the remote sensing of Soil Moisture and Ocean Salinity from a low orbit platform [1]. Results are analyzed with emphasis on stability and error analysis.

This work was supported by the Centre National de la Recherche Scientifique (CNRS) and by the European Space Agency (ESA) within the frame of the SMOS project under contract 17312/03/NL/FF.

1.1. Direct problem

SAIR devoted to Earth observation measure the correlation between the signals collected by pairs of spatially separated antennae A_k and A_l which have overlapping fields of view, yielding samples of the visibility function $V(\mathbf{u})$, also termed complex visibilities, of the brightness temperature map $T(\boldsymbol{\xi})$ of the observed scene. The relationship between $V(\mathbf{u})$ and $T(\boldsymbol{\xi})$ is given by a spatial Fourier-like integral [2]:

$$\begin{aligned} V(\mathbf{u}_{kl}) \propto \frac{1}{\sqrt{\Omega_k \Omega_l}} \iint\limits_{\|\boldsymbol{\xi}\| \leq 1} & F_k(\boldsymbol{\xi}) \overline{F}_l(\boldsymbol{\xi}) T(\boldsymbol{\xi}) \\ \times\, \widetilde{r}_{kl}\Big(\frac{-\mathbf{u}_{kl}\boldsymbol{\xi}}{f_o}\Big) & \, \mathrm{e}^{-2\mathrm{j}\pi \mathbf{u}_{kl}\boldsymbol{\xi}} \frac{\mathrm{d}\boldsymbol{\xi}}{\sqrt{1-\|\boldsymbol{\xi}\|^2}}\,. \end{aligned} \tag{1}$$

The components $\xi_1 = \sin\theta\cos\phi$ and $\xi_2 = \sin\theta\sin\phi$ of the angular position variable $\boldsymbol{\xi}$ are direction cosines (θ and ϕ are the traditional spherical coordinates), $\mathbf{u}_{kl}$ is the spatial frequency associated with the two antennae A_k and A_l (namely, the spacing between the antennae normalized to the central wavelength of observation), $F_k(\boldsymbol{\xi})$ and $F_l(\boldsymbol{\xi})$ are the normalized voltage patterns of the antennae with equivalent solid angles Ω_k and Ω_l (the overbar indicates the complex conjugate), $\widetilde{r}_{kl}(t)$ is the so called fringe-wash function which accounts for spatial decorrelation effects, $t = \mathbf{u}_{kl}\boldsymbol{\xi}/f_o$ is the time delay and f_o is the central frequency of observation.
Denoting by ℓ the number of antennae of the instrument, the number of complex visibilities provided by the interferometer is equal to $\ell(\ell-1)/2$ when accounting for the hermitian property of (1). However, the list of spatial frequencies $\mathbf{u}_{kl}$ is not necessarily non redundant since two different pairs of

antennae may lead to the same spatial frequency.
Since SAIR have limited dimensions, the spatial frequencies $\mathbf{u}_{kl}$ sampled by an interferometer are confined to a limited region of the Fourier domain, the so-called experimental frequency coverage H. Moreover, in many applications they coincide with the nodes of a sampling grid $\mathbb{G}_{\mathrm{u}}$. For example, in the case of SMOS the visibility samples are obtained from raw data inside a star-shaped window over an hexagonally sampled grid in the Fourier domain [1].
For computation purposes, numerical quadrature is used to represent integral (1) as a summation over n^2 integrand samples, here the n^2 pixels of the spatial grid $\mathbb{G}_\xi$ which is the dual grid of $\mathbb{G}_{\mathrm{u}}$. The number of pixels of the grids $\mathbb{G}_{\mathrm{u}}$ and $\mathbb{G}_\xi$ has to be chosen in such a way that the Shannon criterion is satisfied and the numerical quadrature is sufficiently accurate.

1.2. Inverse problem

The inverse problem aims at inverting the discrete version of relation (1) to retrieve the radiometric brightness temperature map T from the complex visibilities V, i.e. solving the linear system:

$$\mathbf{G}T = V, \tag{2}$$

where $\mathbf{G}$ is the discrete (linear) operator from the object space E into the data space F describing the basic relation (1). Since the direct problem is stated via an integral equation, the inverse problem does not usually have a straightforward solution. Moreover, since the dimension of the object space E (here the n^2 pixels used to sample T) is often larger than the dimension of the data space F (the $\ell(\ell-1)/2$ samples of V), the linear system (2) is an underconstrained problem with multiple solutions for T. The minimum of the least-square criterion

$$\min_{T\in E} \|V - \mathbf{G}T\|_F^2, \tag{3}$$

is also the solution of the normal equation $\mathbf{G}^*\mathbf{G}T = \mathbf{G}^*V$. This solution is not unique because the square matrix $\mathbf{G}^*\mathbf{G}$ is singular. According to the definition given by Hadamard [3], the inverse problem is ill-posed and has to be regularized in order to provide a unique and stable solution for T.

2. REGULARIZATION

The problem of retrieving an estimate T_r of the radiometric temperature distribution T of a scene under observation from complex visibilities V has been addressed in [4][5][6]. It has been demonstrated that this inverse problem is ill-posed and has to be regularized in order to provide a unique and stable solution. Two standard "numerical regularizations" and a "physical regularization" are presented here.

2.1. Tikhonov regularization

A standard approach is to find the brightness temperature map T_r that realizes the minimum of the quadratic functionnal [3]

$$\min_{\substack{T\in E\\ \mu\in\mathbb{R}}} \|V - \mathbf{G}T\|_F^2 + \mu\|T\|_E^2 \tag{4}$$

where μ is a Lagrange parameter to be determined prior inversion. For $\mu = 0$ we obtain the discrepancy functionnal (3). The unique solution of (4) is the solution of the Euler equation $(\mathbf{G}^*\mathbf{G} + \mu\mathbf{I})T = \mathbf{G}^*V$ which has to be compared to the normal equation $\mathbf{G}^*\mathbf{G}T = \mathbf{G}^*V$ associated to the least-square criterion (3). This map could be obtained through the computation of the inverse of the non singular square matrix $\mathbf{G}^*\mathbf{G} + \mu\mathbf{I}$:

$$T_r = \mathbf{G}_\mu^+ V, \tag{5}$$

where:

$$\mathbf{G}_\mu^+ = (\mathbf{G}^*\mathbf{G} + \mu\mathbf{I})^{-1}\mathbf{G}^*. \tag{6}$$

The drawback of this numerical approach is the regularization parameter μ because the determination of its optimal value may raise some difficulties.

2.2. Minimum-norm regularization

A second standard approach is to find the minimum-norm solution of (2) by means of computing the temperature map T_r that realizes the minimum of the constrained optimization problem [4][5]

$$\begin{cases} \min\limits_{T\in E} \|T\|_E^2 \\ \mathbf{G}T = V \end{cases} \tag{7}$$

This map could be obtained through the computation of the More-Penrose pseudo-inverse $\mathbf{G}^+$ of the rectangular matrix $\mathbf{G}$:

$$T_r = \mathbf{G}^+ V, \tag{8}$$

where $\mathbf{G}^+$ could be computed with the aid of a standard singular value decomposition [7] of $\mathbf{G}$:

$$\mathbf{G}^+ = \sum_{i\geq 1} \frac{1}{\sigma_i}\mathbf{v}_i\mathbf{u}_i^{\mathrm{T}}. \tag{9}$$

Here, the σ_i's are the singular values of $\mathbf{G}$, written in ascending order, associated to the left and right singular vectors $\mathbf{u}_i$ and $\mathbf{v}_i$. Owing to the particular role played by the smallest σ_i in the computation of $\mathbf{G}^+$, with (9) or with the well-known expression $\mathbf{G}^*(\mathbf{G}\mathbf{G}^*)^{-1}$, it is preferable to compute it with the aid of a truncated singular value decomposition [6][7]

$$\mathbf{G}_m^+ = \sum_{i>m} \frac{1}{\sigma_i}\mathbf{v}_i\mathbf{u}_i^{\mathrm{T}}, \tag{10}$$

so that the regularized minimum-norm solution of (2) is now given by:

$$T_r = \mathbf{G}_m^+ V, \tag{11}$$

where m indicates the number of singular values σ_i discarded prior to inversion. Here again, the drawback of this approach is the choice of the optimal value for m which plays the role of a numerical regularization parameter.

2.3. Band-limited regularization

Referring now to a physical concept, namely the limited resolution of SAIR, another approach is to find the temperature map T_r which has its Fourier transform confined to the experimental frequency coverage H. This band-limited solution realizes the minimum of the constrained optimization problem [6]

$$\begin{cases} \min\limits_{T \in E} \|V - \mathbf{G}T\|_F^2 \\ (\mathbf{I} - \mathbf{P}_H)T = 0 \end{cases} \tag{12}$$

where $\mathbf{P}_H$ is the projector onto the subspace $\mathcal{E}$ (of E) of the H-band limited functions [6]. The unique solution of (12) is given by:

$$T_r = \mathbf{U}^*\mathbf{Z}\mathbf{A}^+V, \tag{13}$$

where:

$$\mathbf{A}^+ = (\mathbf{A}^*\mathbf{A})^{-1}\mathbf{A}^* \tag{14}$$

is the More-Penrose pseudo-inverse of the rectangular matrix $\mathbf{A} = \mathbf{G}\mathbf{U}^*\mathbf{Z}$, $\mathbf{U}$ is the Fourier transform operator and $\mathbf{Z}$ is the zero-padding operator beyond H [6].

3. SIMULATIONS AND RESULTS

Simulations have been performed for a Y-shaped array equipped with 3 antennae per arm in addition to the central one, leading to a total number of antennae and receivers $\ell = 10$. The available number of complex visibilities is here equal to $\ell(\ell-1)/2 = 45$, while there are only 36 spatial frequencies in the star-shaped coverage H. The dimension of the hexagonally sampled grids $\mathbb{G}_\xi$ and $\mathbb{G}_\mathrm{u}$ has been fixed to $n^2 = 256$. The object workspace E is thus isomorphic to $\mathbb{R}^{256}$. Only one measurement of the visibility function for the zero spacing $V(\mathbf{0})$ is included in the modelling operator $\mathbf{G}$. The dual space $\widehat{\mathcal{E}}$ and the data space F are therefore isomorphic to the complex spaces $\mathbb{C}^{36+1}$ and $\mathbb{C}^{45+1}$. However it is more convenient to work in the underlying real spaces $\mathbb{R}^{73}$ and $\mathbb{R}^{91}$. The size of the real-valued matrices $\mathbf{G}$ and $\mathbf{A}$ are therefore 91×256 and 91×73, showing that the linear system (2) is underdetermined while the least-square criterion (12) is overconstrained thanks to the $45 - 36 = 9$ redundant complex visibilities.
The eigenvalues of the real valued square matrices $\mathbf{G}^*\mathbf{G}$ and $\mathbf{G}^*\mathbf{G}+\mu\mathbf{I}$ for $\mu = 10^{-6}$ are shown in Fig. 1. According to the floating point relative accuracy of MATLAB ($\varepsilon \approx 2 \cdot 10^{-16}$), the 165 smallest eigenvalues on the left side of the spectrum should be considered as equal to 0. The number of remaining positive eigenvalues is therefore equal to 91, which is the rank of $\mathbf{G}$. As a consequence, the matrix $\mathbf{G}^*\mathbf{G}$ is singular.

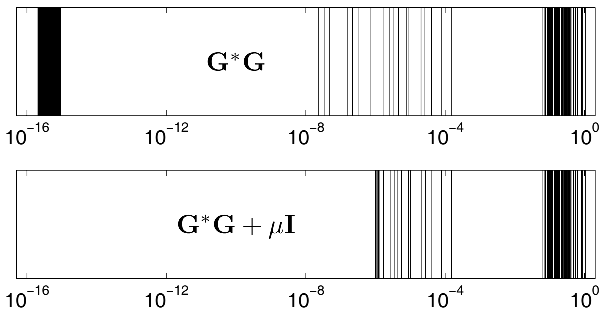

Fig. 1. The 256 eigenvalues of the 256×256 matrices $\mathbf{G}^*\mathbf{G}$ *(top)* and $\mathbf{G}^*\mathbf{G} + \mu\mathbf{I}$ for $\mu = 10^{-6}$ *(bottom)*.

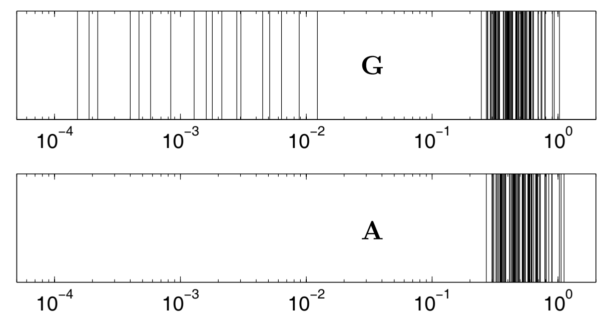

Fig. 2. The 91 singular values of the 91×256 matrix $\mathbf{G}$ *(top)* and the 73 singular values of the 91×73 matrix $\mathbf{A}$ *(bottom)*.

This is not the case of the matrix $\mathbf{G}^*\mathbf{G} + \mu\mathbf{I}$ since its smallest eigenvalue is equal to μ.
The singular values of the real valued rectangular matrices $\mathbf{G}$ and $\mathbf{A}$ are shown in Fig. 2. Both matrices are of full-rank and positive definite. However, it is to be noted that the 73 singular values of $\mathbf{A}$ are of the order of unity. Conversely, the 18 smallest singular values of $\mathbf{G}$ (corresponding to the 9 redundant complex visibilities), out of a total of 91, vary from 10^{-2} down to 10^{-4}. This suggests to compute $\mathbf{G}^+$ with the aid of a truncated singular value decomposition so that these $m = 18$ singular values are discarded prior to inversion, keeping only the $91 - 18 = 73$ largest ones which correspond to the spatial frequencies in the frequency coverage H associated to the unknowns of the overconstrained problem (12).

Complex visibilities have been simulated from a brightness temperature T at its highest level of resolution for an instrument with non identical subsystems (different antennae voltage patterns and different receivers band-pass filters). and a random radiometric noise ΔV with standard deviation $\sigma_{\Delta V} = 0.1$ K has been added on both the real and imaginary parts of V. Reconstructions have been performed in order to compare the Tikhonov solution (5), the regularized minimum-norm solution (11) and the band-limited one (13). Provided that the optimal values for μ and m are used, it turns out that the three methods have the same behaviour with regards to the error propagation: the average factor of noise amplification is

of the order of 0.54 K/K [6].
Concerning the Tikhonov regularization, the choice of the optimal value for the Lagrange parameter μ is a crucial and difficult problem in the theory of regularization. However, one way to find this value is to plot $\|V - \mathbf{G}T_r\|_F$ versus $\|T_r\|_E$ for different values of μ. These variations are shown in Fig. 3 for $10^{-8} \leq \mu \leq 10^{-1}$. As predicted by the theory, the plot has the shape of the letter L (hence the name of "L-curve"). The optimal value for μ corresponds to the point with maximum curvature (i.e. the corner of the L-curve) because it is the best compromise between approximation error and noise propagation. Here it is about 10^{-6} (hence the previous choice of μ in Fig. 1), however this value may depend on the amount of input noise ΔV (here, $\sigma_{\Delta V} = 0.1$ K).
Regarding the minimum-norm regularization, the choice of the number m of singular values σ_i discarded prior to inversion is also a crucial issue. The variations of $\|V - \mathbf{G}T_r\|_F$ with $\|T_r\|_E$ have been reported on Fig. 3 for $1 \leq m \leq 32$. It is worthy of note that the plot has also a L-shaped behaviour and the maximum curvature point, which is very close to the point of the optimal value for μ, corresponds to $m = 18$. The number of singular values kept in the inversion is therefore equal to $91 - 18 = 73$ which is also the previous value suggested by the singular values spectrum shown in Fig. 2.
Finally, we have reported the same quantities for the band-limited solution on the previous L-curves. It can be observed that this point is also very close to the points corresponding to the optimal values for μ and m, which confirms the link between the three approaches, this one having the advantage to have a physical meaning and to be independant from any regularizing parameter.

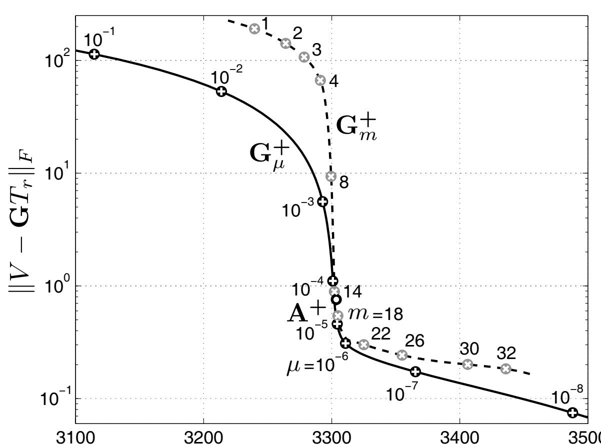

Fig. 3. Variations of $\|V - \mathbf{G}T_r\|_F$ with $\|T_r\|_E$ for the Tikhonov solution (5) with $10^{-8} \leq \mu \leq 10^{-1}$ *(solid line and ⊕)*, the regularized minimum-norm solution (11) with $1 \leq m \leq 32$ *(dashed line and ⊗)* and the band-limited solution (13) *(o marker)*.

4. CONCLUSION

The reconstruction of radiometric brightness temperature maps from complex visibility samples provided by SAIR has been addressed. Since the corresponding inverse problem is ill-posed, it has to be regularized in order to provide a unique and stable solution. Three regularizing methods have been examined, all leading to the same results with regards to the propagation of random radiometric noise. Two of them, the Tikhonov and the minimum-norm approaches, depend on a numerical regularization parameter. The determination of its optimal value is crucial for the behaviour of these methods since non optimal values may lead to large amplification factors of noise. This is not the case of the band-limited approach which does not depend on such a numerical parameter but takes into account the limited resolution of SAIR to regularize the problem. Moreover, the dimension of the system to be solved is reduced to the minimum number of unknowns (or degrees of freedom), the number of frequencies in the experimental frequency coverage, while taking into account, in the least-square sense, all the available complex visibilities without averaging the potentially redundant ones.

5. REFERENCES

[1] Y.H. Kerr *et al.*, "Soil moisture retrieval from space: The soil moisture and ocean salinity (smos) mission," *IEEE Trans. Geosci. and Rem. Sens.*, vol. 39, no. 8, pp. 1729–1735, 2001.

[2] C.S. Ruf *et al.*, "Interferometric synthetic aperture radiometry for the remote sensing of the earth," *IEEE Trans. Geosci. and Rem. Sens.*, vol. 26, no. 5, pp. 597–611, 1998.

[3] M. Bertero and P. Boccacci, *Introduction to Inverse Problems in Imaging*, Institute of physics publishing, 1st edition, 1998.

[4] A.B. Tanner and C.T. Swift, "Calibration of a synthetic aperture radiometer," *IEEE Trans. Geosci. and Rem. Sens.*, vol. 31, no. 1, pp. 257–267, 1993.

[5] M.A. Goodberlet, "Improved image reconstruction techniques for synthetic aperture radiometers," *IEEE Trans. Geosci. and Rem. Sens.*, vol. 38, no. 3, pp. 1362–1366, 2000.

[6] E. Anterrieu, "A resolving matrix approach for synthetic aperture imaging radiometers," *IEEE Trans. Geosci. and Rem. Sens.*, vol. 42, no. 8, pp. 1649–1656, 2004.

[7] C. Hansen, *Rank-Deficient and Discrete Ill-Posed Problems*, Society for industrial & applied mathematics, 1st edition, 1998.